Nanoscale

MINIREVIEW

View Article Online
View Journal | View Issue

Cite this: *Nanoscale*, 2026, **18**, 2475

Gas transformations within metal–organic cages

Federico Tzunux-Tzoc [a,b] and Edmundo G. Percástegui *[a,b]

Received 9th September 2025,
Accepted 24th December 2025

DOI: 10.1039/d5nr03797b

rsc.li/nanoscale

The efficient transformation of gaseous molecules into value-added products remains a central challenge in sustainable chemistry, limited by the low reactivity of some gases and the complexity of achieving product selectivity. Metal–organic cages (MOCs), with their tunable cavities and dynamic host–guest interactions, have emerged as promising platforms for gas conversion, leveraging confinement effects to enhance reactivity and selectivity. This contribution highlights recent advances in MOC-mediated gas transformations—including photocatalytic O_2 reduction, electrochemical CO_2 conversion to combustible gases, H_2S splitting for H_2 generation, and SO_2 oxidation and mineralization—illustrating how spatial arrangement, co-encapsulation of catalysts and substrates, and cavity design unlock new reaction pathways under mild conditions. Mechanistic insights and structural features outline design principles for next-generation cage-based systems. Ultimately, MOCs offer molecular precision to bridge homogeneous and heterogeneous catalysis, with profound implications for the development of complex gas–liquid–solid phase reactions and transformative technologies aimed at addressing some of the most critical challenges in environmental remediation, energy generation, and circular manufacturing.

1. Introduction

As global efforts intensify to mitigate climate change,[1] reduce pollution, and transition toward circular economies,[2,3] the efficient transformation of gaseous molecules into value-

[a]*Universidad Nacional Autónoma de México, Instituto de Química, Ciudad Universitaria, Ciudad de México 04510, Mexico. E-mail: eguzper@unam.mx*
[b]*Centro Conjunto de Investigación en Química Sustentable, UAEM-UNAM, Carretera Toluca-Atlacomulco km 14.5, 50200 Toluca, Estado de México, Mexico*

Federico Tzunux-Tzoc

Federico was born in the small town of Momostenango, Guatemala. He earned his undergraduate degree in chemistry from the University of San Carlos of Guatemala and is currently pursuing a Master's in Chemical Sciences at the National Autonomous University of Mexico (UNAM). His academic journey has centered on supramolecular chemistry, with a particular focus on the design and synthesis of metal–organic cages (MOCs). Under the guidance of Dr G. Percástegui, he has worked on methodologies for synthesizing water-soluble MOCs. Beyond the lab, Federico is deeply interested in theoretical chemistry and the broader physical sciences. In his free time, he enjoys athletics and mountaineering.

Edmundo G. Percástegui

Edmundo was born in Mexico City and earned his Ph.D. in chemistry from the Autonomous University of the State of Hidalgo (UAEH) in Mexico. During his doctoral studies, he spent a year in the group of Darren Johnson at the University of Oregon, investigating self-assembled main-group complexes. He held a DGAPA postdoctoral fellowship in Ivan Castillo's group at the National Autonomous University of Mexico (UNAM), where he worked on metallocalixarenes. From 2016 to 2018, he undertook postdoctoral studies with Jonathan Nitschke at the University of Cambridge, focusing on subcomponent self-assembly and molecular receptors. Later, he was appointed Assistant Professor at the Institute of Chemistry at UNAM. His independent research program, started in 2019, investigates the self-assembly of functional metal–organic containers and supramolecular architectures.

added products has emerged as a critical challenge in modern chemistry. Some gases are abundant, yet often chemically inert,[4] typically requiring high-energy inputs and specialized catalysts for their activation and conversion. Achieving selectivity for the desired products is also challenging, demanding precise control over reaction intermediates and catalytic pathways, particularly in processes involving complex multi-electron and proton transfer steps, or those that encounter competing side reactions. Furthermore, the low solubility of gases in liquids and their slow diffusion in solids limit interactions with catalytic sites.

In recent years, porous materials such as metal–organic frameworks (MOFs)[5,6] and covalent organic frameworks (COFs)[7] have emerged as promising platforms for gas capture and conversion. Their high surface areas, tunable pore environments, and modular architectures allow for selective adsorption and catalytic activation of gaseous substrates. Reticular MOFs and COFs have demonstrated success in CO_2 reduction,[8,9] O_2 activation,[10–12] and other gas-conversion reactions.[13–17] However, their extended frameworks may suffer from limited accessibility of reactants to deeper pores and often lack the molecular precision and dynamic host–guest interactions required to modulate reactivity at the nanoscale, especially under mild and scalable conditions. The strategic design of novel materials is essential for overcoming these limitations and advancing catalysis, renewable energy generation, green chemical manufacturing, and environmental remediation strategies.

Metal–Organic Cages (MOCs)[18]—also referred to as metal–organic polyhedra or coordination capsules—are a notable class of nanomolecular receptors with unique potential for gas capture and transformation. These three-dimensional architectures are formed through the self-assembly of metal ions and organic ligands[19,20] and delineate well-defined internal cavities capable of accommodating a wide range of guest molecules.[21] The host–guest chemistry of MOCs has been extensively explored for diverse applications in both solution and solid state, including molecular recognition,[22–27] sensing,[28–30] separation,[31–33] drug delivery,[34–37] or removal of pollutants.[38–40] More recently, significant attention has been directed toward their use in gas capture and separation.[41–47] Unlike extended frameworks, MOCs offer molecular-level control over cavity size, shape, and functionality, enabling tailored host–guest interactions and confinement effects that can dramatically influence chemical reactivity.[48] The confined space within MOCs isolates guests from bulk environments, increases their local concentrations, and preorganizes them in favorable conformations.[49,50] These confinement effects often lead to significantly enhanced reaction rates and altered product distributions,[51] facilitating chemical transformations that are otherwise inefficient or inaccessible in bulk conditions.[52] Together, these features have recently been harnessed to promote chemical conversions of gaseous substrates within the nanocage spaces. Notably, MOCs have been shown to mediate the photocatalytic reduction of O_2, the electrochemical transformation of CO_2, the light-driven splitting of H_2S, and the oxidation of SO_2.

This minireview highlights the emerging role of MOCs as platforms for gas transformation reactions, focusing on the available examples where molecular confinement within the cage nanocavity plays a decisive role in enhancing reactivity and product selectivity. The selected cases illustrate how the spatial arrangement of catalytic sites, the stabilization of intermediates, the modulation of electronic environments, and the encapsulation of co-catalyst and substrates may lead to the discovery of new reaction pathways and improve catalytic performance. These findings underscore the importance of supramolecular design in achieving efficient gas conversions under mild conditions. Ultimately, the ability of MOCs to confine, activate, and transform gaseous molecules within their nanocavities opens exciting possibilities for future research in catalysis, materials science, and environmental chemistry. As the field continues to evolve, these molecular cages may inspire new strategies for selective gas transformations, bridging the gap between homogeneous and heterogeneous catalysis and offering biomimetic solutions to some of the most pressing challenges in sustainable chemistry.

2. Cavity-mediated gas conversion

The rational design of MOCs, combined with the judicious selection of metal centers, enables the integration of multiple catalytic functions within a single supramolecular framework. In this context, Liu, Lan, and co-workers reported two cobalt-based MOCs—$\mathbf{Co_{14}(L\text{-}H)_{24}}$ and $\mathbf{Co_{14}(L\text{-}CH_3)_{24}}$—capable of simultaneously realizing the oxygen reduction reaction (ORR) and the water oxidation reaction (WOR) for the efficient photocatalytic production of hydrogen peroxide.[53] These MOCs were synthesized *via* the self-assembly of $Co(NO_3)_2{\cdot}6H_2O$ with the ligands HL-H (*N*-benzyl-1-(1*H*-imidazol-4-yl)methanimine) and HL-CH_3 (1-(1*H*-imidazol-4-yl)-*N*-(4-methylbenzyl)methanimine), respectively. Single-crystal X-ray diffraction (SC-XRD) confirmed the formation of rhombic dodecahedral structures with a $[Co^{II}_{14}(L\text{-}R)_{24}]^{4+}$ architecture, comprising 14 Co(II) ions and 24 ligands (Fig. 1a). Two distinct Co(II) coordination environments were identified (inset in Fig. 1a): Co(A), coordinated to four imidazole nitrogen atoms and two water molecules in an octahedral geometry, and Co(B), coordinated octahedrally by six nitrogen atoms from three bidentate ligands. Upon dissociation of the axial water ligands, Co(A) adopts square-planar geometry, exposing an open coordination site that serves as the catalytic center. This structural change also increases the internal cavity diameter from 6.61 Å to 10.93 Å in $\mathbf{Co_{14}(L\text{-}H)_{24}}$ and from 6.55 Å to 10.88 Å in $\mathbf{Co_{14}(L\text{-}CH_3)_{24}}$. In this scenario, water and gaseous O_2 molecules can easily diffuse into the cavity, facilitating the attack of active sites from both inside and outside the cage and promoting improved catalytic activity.

The exchange of ligands at the Co(A) sites is favored, as indicated by the adsorption energies. For water molecules adsorbed on Co(A), the energies are −0.61 eV for $\mathbf{Co_{14}(L\text{-}H)_{24}}$ and −0.48 eV for $\mathbf{Co_{14}(L\text{-}CH_3)_{24}}$, while the adsorption of

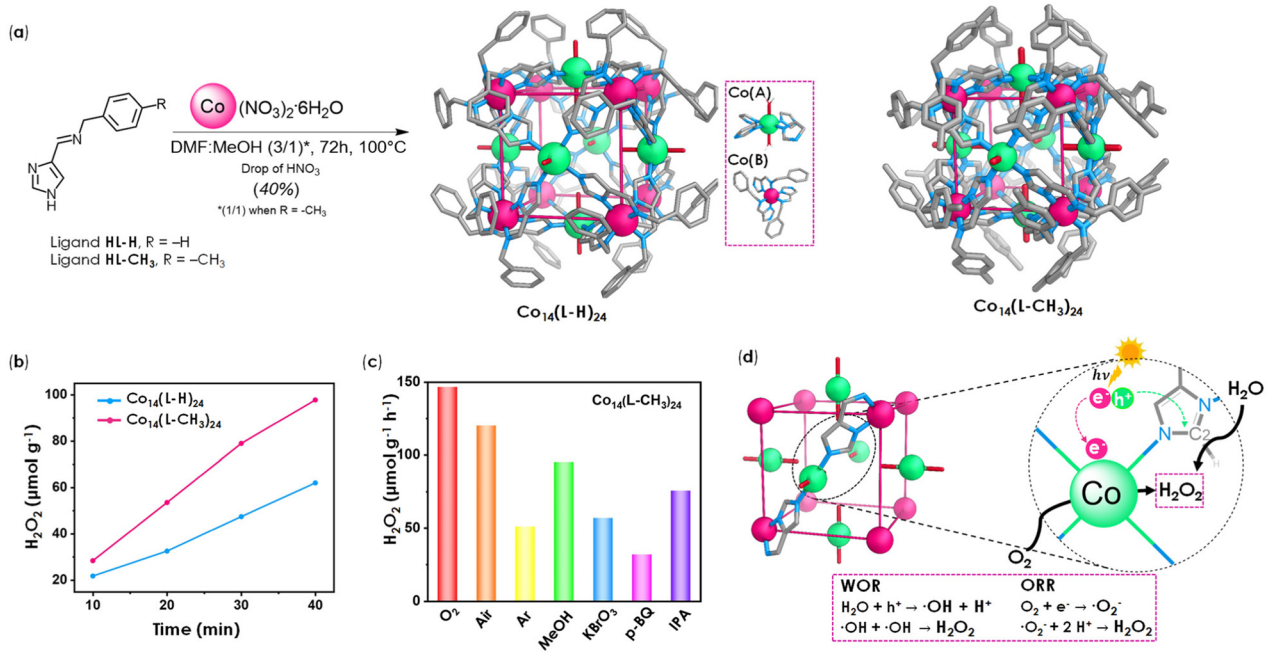

Fig. 1 (a) Schematic representation of the self-assembly of $Co_{14}(L\text{-}H)_{24}$ and $Co_{14}(L\text{-}CH_3)_{24}$ MOCs (hydrogen atoms and counterions are omitted for clarity). (b) Photocatalytic activity for H_2O_2 production in pure water and under O_2 atmosphere. (c) Amounts of H_2O_2 produced in the presence of different agents. (d) The proposed reaction mechanism and the WOR and ORR pathways for photocatalytic synthesis of H_2O_2. Parts (b) and (c) adapted from ref. 53, https://doi.org/10.1002/anie.202308505. Copyright 2023, Wiley-VCH.

oxygen molecules involves energy values of −1.76 eV for $Co_{14}(L\text{-}H)_{24}$ and −1.77 eV for $Co_{14}(L\text{-}CH_3)_{24}$. These values reflect the feasibility of ligand exchange, suggesting that the change in coordination geometry at the Co(A) sites is a dynamic process in which axially bound water ligands are easily replaced by oxygen molecules. These oxygen molecules are reduced, released, and continue the catalytic process. Furthermore, this change in temporary geometry can enhance the utilization of photogenerated electrons at the Co(A) sites. As a result, these sites become more accessible to electrons, which improves the production of $^{\bullet}O_2^-$, a crucial intermediate for the eventual of H_2O_2. UV/Vis-NIR diffuse reflectance spectroscopy revealed that $Co_{14}(L\text{-}CH_3)_{24}$ exhibits broader and stronger light absorption (λ = 300–1100 nm) than $Co_{14}(L\text{-}H)_{24}$. Kubelka–Munk and Mott–Schottky analyses confirmed that both MOCs function as photocatalysts for H_2O_2 generation *via* WOR and ORR. Notably, $Co_{14}(L\text{-}CH_3)_{24}$ possesses a narrower band gap and exhibits approximately twice the transient photocurrent response of $Co_{14}(L\text{-}H)_{24}$, indicating superior charge separation and transport efficiency. These features contribute to its enhanced photocatalytic activity. Photocatalytic H_2O_2 production was evaluated in O_2-saturated pure water under UV/Vis-NIR irradiation (λ = 300–1100 nm), without sacrificial agents, photosensitizers, or pH adjustment. Both MOCs showed time-linear H_2O_2 generation, with $Co_{14}(L\text{-}CH_3)_{24}$ achieving a production rate of 146.60 μmol g^{-1} h^{-1} in 40 min, significantly higher than the 92.91 μmol g^{-1} h^{-1} observed for $Co_{14}(L\text{-}H)_{24}$ (Fig. 1b). Noteworthy, the production of $Co_{14}(L\text{-}CH_3)_{24}$ was approximately 1.6 times higher than that of $Co_{14}(L\text{-}H)_{24}$. Moreover, cycling tests were performed for $Co_{14}(L\text{-}CH_3)_{24}$ and it was found that the H_2O_2 production rate remained virtually unchanged over three consecutive cycles, indicating high stability and durability of the cages.

Mechanistic studies were implemented to elucidate the reaction pathways involved in the production of H_2O_2 (Fig. 1c). For instance, under an Ar-saturated atmosphere (without O_2 gas), only a small amount of H_2O_2 was produced (36.51 μmol g^{-1} h^{-1} for $Co_{14}(L\text{-}H)_{24}$ and 50.77 μmol g^{-1} h^{-1} for $Co_{14}(L\text{-}CH_3)_{24}$). These and other results corroborated that H_2O and O_2 are essential for H_2O_2 production. In a model experiment, using $H_2{}^{18}O$ and $^{16}O_2$, the photocatalytically-synthesized H_2O_2 decomposed by MnO_2 and yielded a product consisting of $^{16}O_2$ and $^{18}O_2$ in a 1 : 1 ratio, indicating that both H_2O and O_2 are the raw materials for the photocatalytic synthesis of H_2O_2. To gain greater insights into the mechanism of WOR and ORR reactions, 1,4-benzoquinone (*p*-BQ) and isopropanol (IPA) were added to the H_2O_2 synthesis system as reagents to capture $^{\bullet}O_2^-$ and $^{\bullet}OH$, respectively. In the presence of *p*-BQ and IPA, the production rate for each of the cages decreased (Fig. 1c), indicating that both $^{\bullet}O_2^-$ and $^{\bullet}OH$ are reactive intermediates, with $^{\bullet}O_2^-$ playing a fundamental role in the ORR pathway. Density functional theory (DFT) calculations supported that H_2O molecules adsorb onto the imidazole fragments, forming non-conventional hydrogen bonds with the C2–H group (WOR site), while O_2 gas molecules are adsorbed and activated at the Co(A) ions, the ORR catalytically active sites. The mechanism of H_2O_2 synthesis and the WOR and ORR pathways is illustrated in Fig. 1d.

This study demonstrated, for the first time, the potential of MOCs as integrated photocatalysts, leveraging confinement effects, for H_2O_2 synthesis. The spatial arrangement of redox-active sites, for both ORR and WOR processes, within the same cage framework enhances host–guest interactions, facilitates contact between reactants and catalytic sites, and shortens the pathway for photogenerated charges, enabling their rapid transfer. The cage design also gathers six octahedral cobalt(II) Co(A) sites that allow for the simultaneous fixation of multiple gas molecules into the cavity. This arrangement ensures internal oxygen binding, enhances the interaction between the gas and the catalyst, and boosts the production rate of H_2O_2.

The increasing concentration of atmospheric CO_2 is a major contributor to climate change, prompting urgent efforts to develop sustainable strategies for its mitigation. One promising approach is the catalytic conversion of CO_2 into value-added chemicals, which not only reduces greenhouse gas emissions but also contributes to a circular carbon economy and a more sustainable chemical industry. Among emerging approaches, MOCs have demonstrated in recent years their potential as promising platforms for CO_2 transformation due to their tunable structures and ability to promote unique reactivity within their confined molecular environments. Earlier this year, Zhang and coworkers reported that the boron–imidazolate cage **BIC-145** facilitates the electrochemical reduction of CO_2 into various products, with ethylene (C_2H_4) being the predominant one.[54] Ethylene is industrially significant due to its high economic value as a precursor in polymer manufacturing.

Cage **BIC-145** was obtained from the solvothermal reaction between the KBH(bim)$_3$ (bim = benzimidazole) ligand salt (L) and Cu(NO$_3$)·3H$_2$O, in the presence of L-tyrosine and a mixed solvent system comprising H_2O, DMSO and *t*-BuOH, heated at 80 °C. The resulting $[Cu^I_6L_4]^{2+}$ cage was confirmed by SC-XRD to be a regular molecular octahedron defined by the six Cu(I) ions crystallizing in the orthorhombic space group $F\bar{4}3c$ (Fig. 2a). The choice of KBH(bim)$_3$ was strategic, as it provides a robust Cu–N coordination bond and a strong B–N covalent bond, conferring stability across various solvents (i-PrOH, H_2O, MeOH, DMF, EtOH, *t*-BuOH) and a broad pH range ($1 \leq pH \leq 14$). **BIC-146**, an isostructural but less symmetric variant of **BIC-145** was obtained by altering the solvent composition to H_2O : DMSO : EtOH during the self-assembly reaction. **BIC-146** crystallizes in the $P\bar{1}$ space group; both MOCs share the $[M_6L_4]$ octahedral array defined by the six Cu atoms. A peculiarity of these two cages is that during formation, the Cu(II) ions reduced to Cu(I) ions as was verified by X-ray photoelectron spectroscopy. Furthermore, **BIC-145** was confirmed by mass spectrometry studies in which the signal detected at m/z = 1730.8983 confirmed the $\{Cu^I_6[BH(bim)_3]_4(H_2O)_{33}\text{-}(DMSO)_{13}\}^{2+}$. Electrochemical performance was evaluated in an H-type cell using glassy carbon working electrode and KCl : Cs_2CO_3 (0.1 M/0.05 M) as electrolytes. The main carbon products were CO, CH_4, C_2H_4, and HCOOH, with product distribution strongly dependent on the applied potential (Fig. 2b). At −1.1

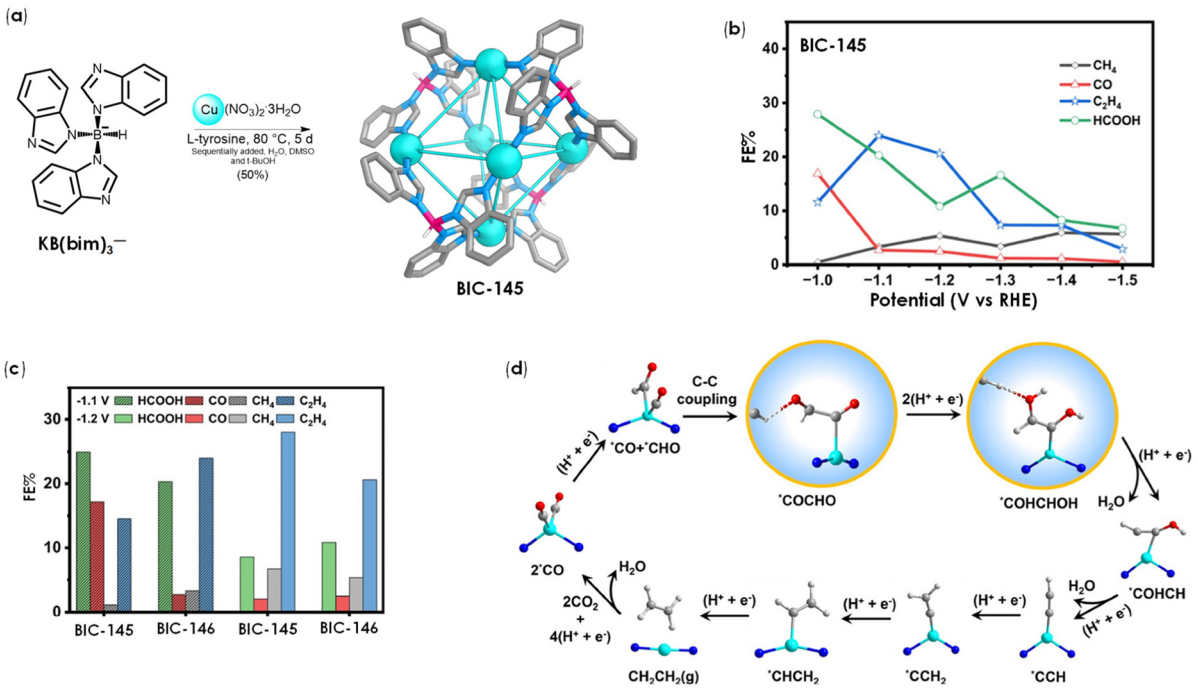

Fig. 2 (a) Schematic process of self-assembly of $BH(bim)_3^-$ and Cu(II) ions to produce **BIC-145**. (b) The FE of valuable gas and liquid products of **BIC-145** electrocatalyst at different applied potentials. (c) Comparison of valuable carbon products from **BIC-145** and **BIC-146** at −1.2 and −1.1 V *vs.* RHE. (d) The possible electrochemical pathways to reduce CO_2 to C_2H_4 showing key intermediates adsorbed on the Cu site inside the **BIC-145** cage. Parts (b–d) adapted from ref. 54, https://doi.org/10.1007/s11426-024-2290-5. Copyright 2025, Springer Nature.

V, **BIC-145** predominantly produced C_2H_4 and CO, while at −1.2 V, CO formation decreased and C_2H_4 remained the major product (Fig. 2c). **BIC-146** exhibited lower selectivity for C_2H_4, with faradaic efficiencies of 24.0% at −1.1 V and 20.6% at −1.2 V, compared to **BIC-145**. A key difference between the two MOCs lies in their electrochemical stability. At a potential of −1.2 V, **BIC-145** displayed exceptional stability, maintaining a stable current density (−3.54 mA cm^{-2}) over 5 h of electrolysis, while **BIC-146** exhibited declining performance after 2 h under the same conditions. This difference is attributed to the higher symmetry and well-ordered configuration of **BIC-145**, which enables it to withstand structural deformations caused by the coordination or adsorption of intermediates in its cavity that are produced during CO_2 reduction to C_2H_4. In contrast, the lower structural symmetry of **BIC-146** was inferred to result in weaker host–guest associations with the intermediates. Thus, not only the Cu(I) active sites (where the intermediates are coordinated) are key in catalysis, but also the structural configuration of the cage cavity is crucial for catalytic performance, particularly in the adsorption and stabilization of intermediates in the cavity during CO_2 reduction.

Density functional theory (DFT) calculations further elucidated the mechanism. An active Cu(I) site coordinates with two CO molecules to form two activated *CO intermediates, transitioning from a linear Cu(I) to a distorted tetrahedral ion (Fig. 2d); the Cu(I) site exhibits strong affinity for CO. Moreover, DFT suggested that the Cu(I) center, in synergy with the boron-imidazolate ligands, aids the formation of the *COCHO intermediate from *CO and *CHO, a key intermediate influencing the selectivity for C_2H_4. The authors proposed that this intermediate is stabilized by a non-classical hydrogen bond between the C–H bond of the aromatic ring adjacent to the N atoms of the imidazolate ligand and the oxygen of *COCHO, as well as the coordination between the Cu(I) site and a carbon atom of *COCHO within the cage. In this example, the size, polarity, and shape of the cage cavity critically modulate activation barriers for CO_2-to-C_2H_4 conversion by tailoring the microenvironment around the active Cu(I) sites. The large, flexible cavity (~10 Å diameter) reduces steric hindrance, enabling co-adsorption of *CO and *CHO intermediates and facilitating C–C coupling events, overcoming a relatively low barrier (1.15 eV). The cavity polarity from boron–imidazolate ligands and open Cu coordination sites increases affinity for CO, which in turn, may promote strong σ–π back bonding and non-classical hydrogen bonding, stabilizing key intermediates (*e.g.*, *COCHO) and lowering energy penalties during hydrogenation steps. Thus, the confinement effect operates through (i) spatial restriction, enforcing proximity and orientation of reactants for efficient coupling; (ii) electronic modulation, where ligand fields and Cu–B interactions tune adsorption energies; and (iii) intermediate stabilization, *via* hydrogen bonding between key and reactive intermediates and cage walls, which minimizes conformational distortion and preserves catalyst integrity. Collectively, these factors reshape the reaction pathway, favoring ethylene formation over competing routes.

The strategic design of MOCs for gas capture and transformation can be significantly enhanced by integrating them into highly porous systems that feature multiple permanent voids. One promising approach involves embedding MOCs within porous liquids (PLs)—a unique class of fluids characterized by intrinsic, permanent cavities. Such a combination offers a compelling solution to the limited gas solubility typically observed in conventional porous solids, particularly in applications involving gas–liquid–solid phase reactions. In a notable example, He *et al.* reported the synthesis of a porous liquid based on MOCs, capable of storing and activating CO_2 molecules within its permanent cavities, thereby facilitating the synthesis of formamide derivatives.[55] The porous liquid was obtained by combining the calixarene-like ligand H_4TBSC, $Zn(NO_3)_2{\cdot}6H_2O$, and PEG-Im-BDC. Notably, PEG-Im-BDC features long polyethylene glycol (PEG) chains with a molecular weight of *ca.* 4000 g mol^{-1} and a length of ≈13 nm, which play a crucial role to preserve the hollow architecture in the liquid phase. The resulting MOC, **Im-PL-Cage** (Fig. 3a), was obtained as a viscous, paste-like material at room temperature, with a melting point of ≈58 °C, rendering it liquid under mild conditions. FT-IR and UV-vis analyses suggested deprotonated carboxylate groups, demonstrating that the PEG-Im-BDC ligand is fully coordinated to the zinc metal centers. The crystal structure of **Im-PL-Cage** was not obtained; however, the analogous **Zn-Cage** structure was elucidated using the ligand (5-Meim-1,3-H_2BDC)$^+$(Cl^-), which lacks the long PEG chains (Fig. 3a). The **Zn-Cage** was characterized by SC-XRD, PXRD, and mass spectrometry, supporting the proposed model of **Im-PL-Cage** (Fig. 3a). The barrel-shaped *endo* cavity of the **Zn-Cage** features two small portals of 6.8 × 4.5 $Å^2$ (including van der Waals radii), which are large enough to permit CO_2 ingress while excluding the bulky PEG chains. This structural array ensures that the cavity of **Im-PL-Cage** remains permanently unoccupied and that the imidazolium active sites are accessible for CO_2 interaction during catalysis. Thermogravimetric analysis (TGA) further confirmed the thermal stability of **Im-PL-Cage** up to 200 °C, with no significant weight loss, indicating that no volatile solvent molecules remained within cage cavities. Molecular dynamics simulations corroborated the presence of pores in **Im-PL-Cage** ranging from 4 to 6 Å, which were readily penetrated by CO_2 molecules (Fig. 3b). The permanent cavity of **Im-PL-Cage** was reflected in its adsorption CO_2 capacity (1.78 mmol g^{-1} at 10 bar, Fig. 3c). Importantly, even after the removal of external CO_2 pressure, a substantial fraction of the gas remained sequestered within the porous **Im-PL-Cage**. In contrast, although **Zn-Cage** also showed high CO_2 uptake, it released most of the adsorbed CO_2 upon depressurization, rendering it less effective for downstream formylation reactions.

Beyond gas storage, the activation of CO_2 is desirable to form new compounds with added value. For this purpose, the confined CO_2 was used as a gas source for reductive *N*-formylation reactions. The CO_2 stored in the pores can be easily accessed and activated by the imidazolium sites near the cage walls and the subsequent reaction with amine substrates. To achieve this, first, the CO_2 was loaded into **Im-PL-Cage** at

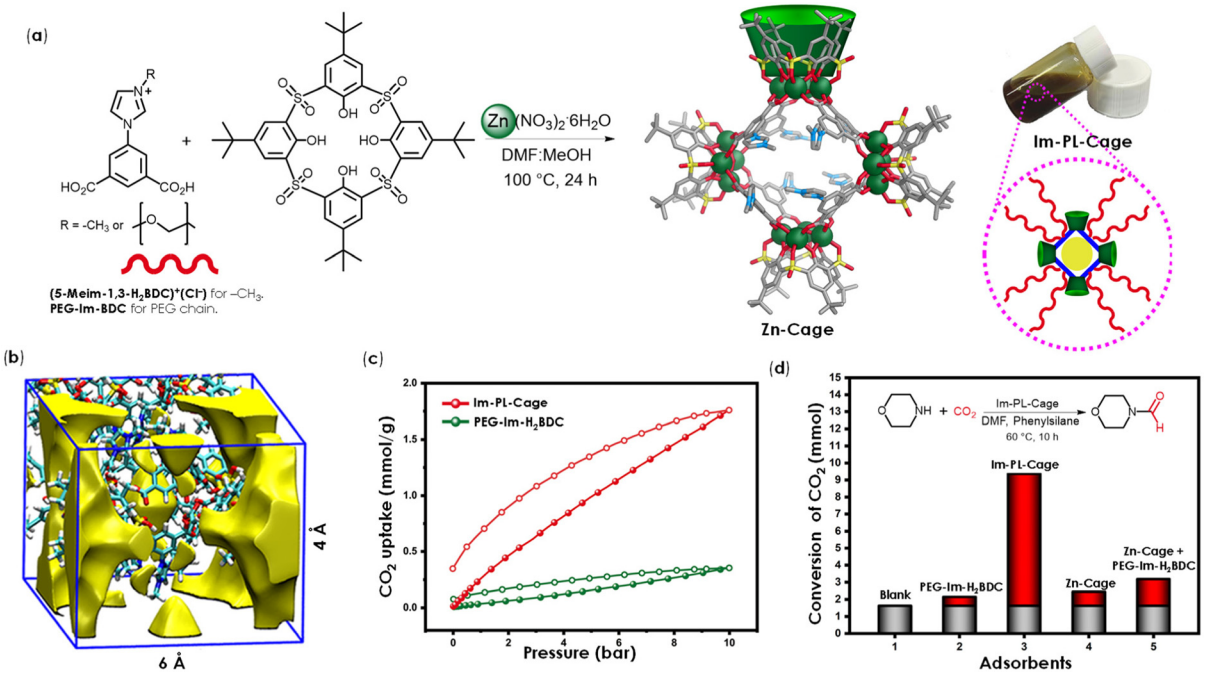

Fig. 3 (a) Schematic process of self-assembly to produce **Zn-Cage** and porous liquid **Im-PL-Cage**. (b) Snapshots of simulation boxes for **Im-PL-Cage** and pore space in **Im-PL-Cage**. (c) CO_2 adsorption–desorption isotherms of **PEG-Im-H$_2$BDC** and **Im-PL-Cage** at ambient temperature. (d) The formylation reaction of morpholine with CO_2 and phenylsilane. Gray bars represent the transformed amount of CO_2 that occupied the reactor, and red bars represent the transformed amount of CO_2 that was adsorbed on different absorbents. Parts (b–d) adapted from ref. 55, https://doi.org/10.1038/s41467-023-39089-x. Copyright 2023, Springer Nature.

20 bar until saturation, followed by equilibration to atmospheric pressure. Subsequently, amine substrates and phenylsilane were introduced, they reacted with the stored CO_2 and then released from the **Im-PL-Cage** at 60 °C in an air atmosphere. As a proof of concept, morpholine was used as a substrate that reacted with a high concentration of CO_2 (7.74 mmol) in **Im-PL-Cage** to give *N*-formylmorpholine in a high yield of 96.7% (Fig. 3d). This high conversion is attributed to the permanent porosity of **Im-PL-Cage**, which allows CO_2 confinement at levels nearly 15-fold higher than pure PEG-Im-H$_2$BDC. Conversely, **Zn-Cage** afforded only 24.5% under identical conditions, likely due to rapid CO_2 desorption during decompression.

The long PEG chains in **Im-PL-Cage** aid in retaining CO_2 and enhancing its reactivity with morpholine. Additional amine substrates were also tested for formylation, achieving good to excellent conversion rates, indicating that the catalyst has a broad substrate compatibility. Furthermore, **Im-PL-Cage** displayed good recyclability, maintaining 93% yield of *N*-formylmorpholine after five consecutive cycles. Hence, the cavity of the MOC governs CO_2 activation by integrating polarity from imidazolium sites with confinement effects. CO_2 is captured near these sites, where spatial restrictions keep the molecule in a reactive state for subsequent conversion and minimize diffusion entropy. Meanwhile, the charged inner walls exert strong electronic modulation, stabilizing CO_2 transition states. Importantly, this confinement reshapes the reaction pathway through synergistic effects that also occur within the pores of the neat liquid, enabling efficient formylation with high yield and material recyclability. With its unique combination of permanent porosity, fluidity, and catalytic efficiency due to molecular confinement, **Im-PL-Cage** bridges the advantages of heterogeneous and homogeneous systems, offering facile mass transfer, high reactivity, and reusability, thereby expanding the horizon for catalytic applications.

MOCs are emerging and versatile platforms for gas transformation reactions, not only due to their ability to confine and concentrate gaseous molecules within well-defined cavities, but also because they can co-encapsulate other reactive species such as substrates and catalysts. By confining gases, substrates, and catalytic centers into close proximity, these MOCs generate unique nanoenvironments that enhance reaction rates, improve selectivity, and stabilize reactive intermediates, unlocking synergistic effects that extend far beyond simple gas capture. In 2025, Sun, Wang *et al.* reported an elegant example in which two MOCs, **Cu$_3$VMOP** (empty) and its host–guest derivative, the host–guest **Cu$_4$I$_4$@Cu$_3$VMOP** containing a Cu_4I_4 cluster in its cavity, catalyze the photoreduction of CO_2 with different product selectivity. While empty **Cu$_3$VMOP** catalyzes the reduction of CO_2 to HCOOH and CH_3COOH as main products, the host–guest **Cu$_4$I$_4$@Cu$_3$VMOP** photocatalyst affords exclusively HCOOH in much higher yield than the free-cluster cage.[56] Typically, the photochemical reduction of CO_2 is fundamentally characterized by a multi-electron and proton transfer process, and selectivity remains a crucial challenge.[57] In this regard, it is essential to obtain highly selective catalysts in the reduction process. Crystals of

tetrahedron **Cu_3VMOP** were obtained through one-pot reaction of $VOSO_4{\cdot}xH_2O$, the ligand 1*H*-pyrazole-4-carboxylic acid (H_2PA), and $Cu(NO_3)_2$ in DMA : MeOH at 130 °C. The H_2PA ligand was intentionally chosen to enable selective coordination of the carboxylate group with the strongly acidic polyoxovanadates, whereas the pyrazolate moiety coordinates with the less acidic copper ions, enabling the assembly of a heterometallic MOC. To construct the *endo*-functionalized **Cu_4I_4@Cu_3VMOP** cage, the Cu_4I_4 cluster was formed *in situ* within **Cu_3VMOP** by introducing pyridyl-4-phosphonic acid and an additional copper source, CuI. The molecular framework of **Cu_3VMOP** contains two types of secondary building units (SBUs): a polyoxovanadate cluster $\{V_6S\}$ and a trinuclear copper cluster $\{Cu_3Pz_3\}$ (Fig. 4a). The $\{Cu_3Pz_3\}$ unit is structurally analogous to 1,3,5-tris(4-carboxyphenyl)benzene (H_3BTB). Overall, **Cu_3VMOP** features four 3-connected vertices $\{V_6S\}$ and four 3-connected $\{Cu_3Pz_3\}$ faces. On the other hand, **Cu_4I_4@Cu_3VMOP** possesses four 3-connected vertices $\{V_6P\}$ and four 3-connected $\{Cu_3Pz_3\}$ faces. The $\{V_6P\}$ corner is analogous to $\{V_6S\}$ where the phosphonate groups of pyridine phosphonate ligands replace the sulfate at the center of the $\{V_6S\}$ cluster. The crystal structures of **Cu_3VMOP** and **Cu_4I_4@Cu_3VMOP** were confirmed by SC-XRD (Fig. 4a) and PXRD, with experimental patterns matching simulated ones. X-ray photoelectron spectroscopy (XPS) revealed that the Cu ions in the Cu_4I_4 cluster maintain a +1-oxidation state, whereas those in $\{Cu_3Pz_3\}$ faces remain at oxidation states of +2. Photocatalytic CO_2 reduction experiments were carried out using $Ru(bpy)_3Cl_2$ as the photosensitizer and triethanolamine (TEOA) as the sacrificial agent in CH_3CN solution. Noteworthy, no reduction products were detected during control experiments using VMOP-15, an isostructural MOC composed of BTB and copper-free $\{V_6S\}$. Upon replacing VMOP-15 with **Cu_3VMOP** and irradiating for 3 h, formic acid (HCOOH) and acetic acid (CH_3COOH) were detected as the major products at yields of 2.5 and 0.9 mmol g^{-1}, respectively (Fig. 4b). Remarkably, when **Cu_4I_4@Cu_3VMOP** was used as a catalyst under identical conditions, a selective conversion of CO_2 to HCOOH was noted with 100% selectivity and an enhanced yield of 10.5 mmol g^{-1}, exceeding that of **Cu_3VMOP** by a factor of 4.2 times. The host–guest catalysts also showed outstanding stability and efficiency over multiple and consecutive catalytic cycles. Undoubtedly, the confinement of the Cu_4I_4 cluster within **Cu_3VMOP** significantly alters the electronic properties of the catalyst, playing a key role in directed electron/substrate migration and intermediate anchor and stabilization. Mechanistic investigations combining femtosecond transient absorption (fs-TA) and DFT calculations revealed that the Cu_4I_4 cluster enhances localized electronic states and modulates orbital configurations, thereby alleviating charge recombination and extending a long-lived charge-separated state. The fs-TA results reveal a significantly longer absorption decay half-life of the excited state of **Cu_4I_4@Cu_3VMOP** (τ_1 = 9.38 ps, τ_2 = 104.90 ps) compared to **Cu_3VMOP** (τ_1 = 0.92 ps, τ_2 = 37.53 ps). This extended lifetime improves photogenerated charge separation efficiency and extends the excited state, ultimately favoring the photocatalytic process. The *in situ* DRIFTS spectra of **Cu_3VMOP** showed peaks at 1507 cm^{-1} for *OCHO, a crucial intermediate for HCOOH, as well as bands at 1558 cm^{-1} and 1540 cm^{-1} for *COCO and for *COOH, key intermediates associated with the production of CH_3COOH. In contrast, for **Cu_4I_4@Cu_3VMOP**, the intensity of the *OCHO

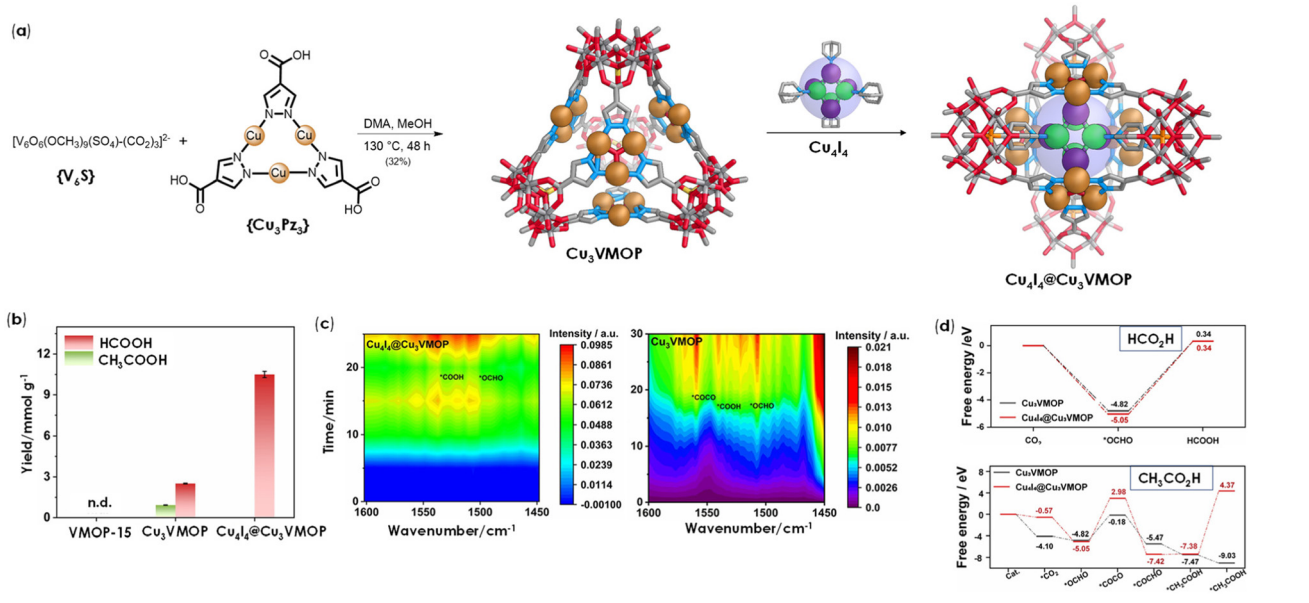

Fig. 4 (a) Sequential self-assembly of **Cu_3VMOP** and **Cu_4I_4@Cu_3VMOP**. (b) Comparison of yields and selectivity observed for the relevant catalysts during the CO_2 reduction reactions. (c) *In situ* DRIFTS spectra for detecting the reaction intermediates on **Cu_4I_4@Cu_3VMOP** and **Cu_3VMOP**. (d) Free-energy diagrams for HCOOH and CH_3COOH for **Cu_3VMOP** and **Cu_4I_4@Cu_3VMOP**. Parts (b–d) adapted from ref. 56, https://doi.org/10.1002/anie.202423018. Copyright 2025, Wiley-VCH.

peak (1506 cm^{-1}) gradually increased with time, while the signals related to C–C coupling were not observed (Fig. 4c). Electrostatic potential analysis from theoretical simulations indicated that the negative charges were mainly concentrated on $\{V_6S\}$ clusters in **Cu_3VMOP**, whereas in **Cu_4I_4@Cu_3VMOP**, they are distributed across both $\{V_6P\}$ and Cu_4I_4 clusters, suggesting that Cu_4I_4 may act as an electron trap to generate the localized electronic excited states. HOMO and LUMO calculations identified the $\{Cu_3Pz_3\}$ fragments as the catalytic site for CO_2 reduction in both cage systems, with the charge recombination being efficiently suppressed by Cu_4I_4. An essential requirement for efficient substrate catalysis is the stereospecific orientation and complementarity between substrates (and/or intermediates) and the catalytic site, which ensures favorable energy barriers. Analogous to enzymatic systems, it was observed that the **Cu_4I_4@Cu_3VMOP** cluster slightly decreases the activation energy of the rate-determining step for obtaining formic acid (*OCHO → HCOOH), from −4.82 eV in **Cu_3VMOP** to −5.05 eV. This reduction in the activation energy barrier suggests that **Cu_4I_4@Cu_3VMOP**, similar to enzymes and with the confined Cu_4I_4 complex makes HCOOH generation more favorable (Fig. 4d). Furthermore, **Cu_4I_4@Cu_3VMOP** exhibited a significantly higher energy barrier for *CO coupling (+8.03 eV, endothermic), which inhibits acetic acid formation and enhances formic acid selectivity. On the other hand, **Cu_3VMOP** displayed a lower energy barrier (+4.64 eV), favoring the C–C bond formation (Fig. 4d). The tetrahedral cavity of **Cu_3VMOP** and its *endo*-functionalized variant **Cu_4I_4@Cu_3VMOP** mimic enzymatic active sites, where cavity size and geometry enforce substrate preorganization, while polarity from embedded clusters modulates electron density. This dual control lowers activation barriers for single-carbon products and selectively raises those for C–C coupling, steering the reaction toward formic acid. The endogenous Cu_4I_4 clusters act as electron traps, suppress charge recombination, prolonging charge-separated states, and stabilizing *OCHO intermediates, akin to cofactor-assisted catalysis in metalloenzymes. Such biomimetic confinement parallels molecular sieving phenomena, demonstrating how cavity architecture–through shape, polarity, and electronic tuning–may dictate catalytic selectivity and efficiency in gas conversion reactions.

As demonstrated in previous examples, molecular confinement within well-defined cavities—reminiscent of enzymatic active sites—can significantly enhance substrate activation and electron transfer through synergistic co-encapsulation of substrates and host–guest interactions.[58,59] Another compelling demonstration of this concept is MOC **H1**, a homogeneous electrocatalyst whose inner nanoenvironment encapsulates and activates the *in situ* formed ethanolamine-CO_2 adduct. This confinement-driven activation enables CO_2 reduction to methane at a record-low overpotential.[60] MOC **H1** is obtained from the equimolar reaction of $Fe(OTf)_2$ with a tridentate–bidentate ligand containing guanidine groups under inert conditions (Fig. 5a). SC-XRD analysis evidenced a tetrahedral

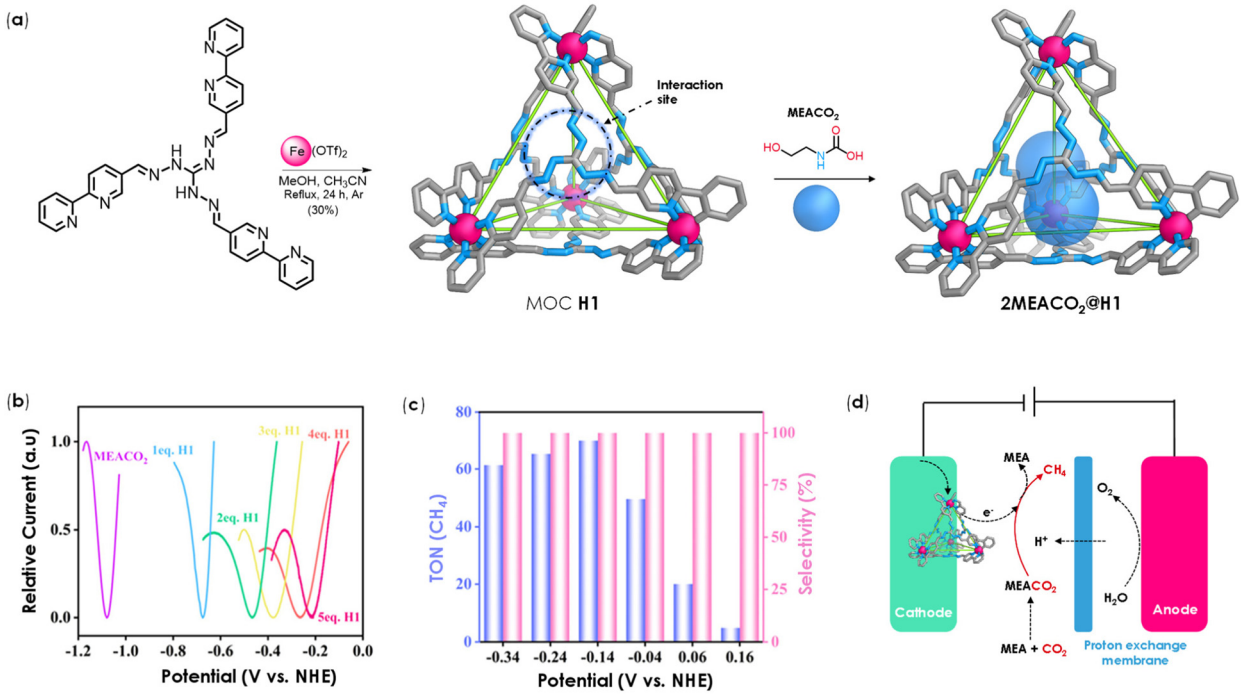

Fig. 5 (a) Schematic process of self-assembly to produce **H1** and the formation of the host–guest **2$MEACO_2$@H1** adduct. (b) Square wave voltammetry (SWV) of the systems containing $MEACO_2$ (0.1 mM) at different concentrations of **H1**. (c) Relationship between TON and selectivity for the electrocatalytic reduction of CO_2 to CH_4 by **H1** at different controlled potentials. (d) Schematic diagram of the cavity-mediated mechanism for the conversion of $MEACO_2$ into CH_4 within tetrahedron **H1**. Parts (b–d) adapted from ref. 60, https://doi.org/10.1039/d5qi00756a. Copyright 2025, The Royal Society of Chemistry.

$[Fe^{II}_4L_4]^{8+}$ molecular array, in which each Fe(II) center is coordinated by three bidentate N,N′-ligand arms, resulting in a symmetric and robust architecture. The molecular array persists in solution as confirmed by NMR and mass spectrometry studies. The guanidine groups in **H1** activate hydrogen bonding with guest molecules. In particular, the adduct formed *in situ* by ethanolamine and CO_2 (**MEACO$_2$**) could be stabilized by hydrogen bonds within **H1** as confirmed by ESI-MS, which showed a peak at m/z = 784.8828, assigned to $[Fe_4L_4(OTf^-)_2{\cdot}(MEACO_2^-)_2]^{4+}$. Likewise, Isothermal Titration Calorimetry (ITC) further validated the encapsulation of two **MEACO$_2$** units, with a favorable Gibbs free energy change (ΔG = −31.53 kJ mol^{-1}). Electrochemical studies using square wave voltammetry (SWV) revealed a dramatic positive shift in the reduction potential of **MEACO$_2$** from −1.10 V to −0.21 V *vs.* the normal hydrogen electrode (NHE) upon encapsulation by **H1** (Fig. 5b), indicating strong host–guest interactions that facilitate electron transfer and activation. Electrocatalytic reduction experiments were conducted under CO_2-saturated and standard conditions (gas bubbled until saturation, DMSO/H_2O = 2 : 1, 0.1 M LiCl, 2.0 M ethanolamine, 0.01 mM Cage **H1**). CH_4 production was observed across a wide potential range, with significant generation at 0.16 V *vs.* NHE registered at the cathode and oxygen-evolution taking place at the anode. As the cathodic potential decreased, both faradaic efficiency and turnover frequency (TOF) significantly increased, while CH_4 selectivity remained near 100% (Fig. 5c). For further experiments at −0.04 V *vs.* RHE, continuous electrocatalysis over 18 hours maintained 100% selectivity and yielded a faradaic efficiency of 69.8% and a turnover number (TON) exceeding 220. To demonstrate the role of confinement and guanidine functionality, a molecular complex **M1** was synthesized as a control catalyst, consisting of Fe(II) coordinated by three 2,2′-bipyridine ligands. SWV studies indicate that **M1** shows minimal **MEACO$_2$** activation, with a negligible shift in reduction potential (from −1.08 V to −1.02 V *vs.* NHE), underscoring the essential importance of the **H1** nanoenvironment and guanidine groups in catalytic performance. *In situ* Raman spectroscopy provided mechanistic insights, identifying a signal at 675 cm^{-1} corresponding to MEA-COO$^-$*, which is a key intermediate in the reduction of CO_2 to CH_4. Likewise, absorption peaks were detected at 1047 cm^{-1} (MEA-COOH*) and at 2921 cm^{-1} (MEA-CH_3) that increased over time. The proposed mechanism involves electron transfer to **MEACO$_2$** within the **H1** cavity, facilitating the gradual hydrogenation to $MEACH_3$*, a process followed by the cleavage of the C–N to release CH_4, and regeneration of the ethanolamine–CO_2 adduct, completing the catalytic cycle (Fig. 5d). This study highlights how molecular confinement within MOCs, in this case, a guanidine-based tetrahedron, is central to steering the CO_2-to-CH_4 conversion by creating a microenvironment that mimics enzymatic active sites. Spatial restriction inside the cage preorganizes the ethanolamine–CO_2 adduct, ensuring proximity between reactive centers and facilitating stepwise hydrogenation while suppressing competing C–C coupling reactions. Simultaneously, the polar guanidine groups and hydrogen-bonding interactions electronically modulate the substrate, lowering the reduction potential by nearly 0.9 V compared to the free adduct and stabilizing key anionic intermediates, thus offering a biomimetic strategy for selective and efficient carbon conversion.

Hydrogen sulfide (H_2S) is a toxic and corrosive gas commonly found in industrial waste streams and natural sources such as geothermal vents and crude oil. Its efficient transformation into benign or valuable products is a pressing challenge in environmental chemistry and sustainable catalysis. One promising strategy could involve leveraging confinement effects within supramolecular architectures to enhance reactivity and selectivity. In 2017, Duan, He, Reek *et al.* informed that the redox-active **Ni-TFT** cage encapsulates the organic dye fluorescein (FL), such a host–guest complex (**FL@Ni-TFT**) was applied for light-driven splitting of H_2S, generating molecular hydrogen and elemental sulfur.[61] The combination of 6 equiv. of $Ni(CH_3COO)_2{\cdot}4H_2O$ with 4 equiv. of the 2,2,2-((nitrilotris(benzene-4,1-diyl))tris(methanelylidene))tris(hydrazinecarbothioamide) ligand (**H_3TFT**) in DMF afforded **Ni-TFT**. The resulting molecular octahedron features Ni(II) ions at the vertices of the array and **H_3TFT** ligands spanning the faces, with two ligands positioned on opposite faces (Fig. 6a). The high coordination capacity of the sulfur-containing **H_3TFT** ligands confers exceptional stability to MOC **Ni-TFT**, even in the presence of sulfide ions, which are known to strongly coordinate to metals, leading to poisoning or decomposition of the metal catalyst. Furthermore, the amino groups of the building blocks can act as hydrogen bond acceptors and donors, while phenyl rings enable π–π stacking associations, collectively acting in favor of effective fluorescein binding (Fig. 6a). ESI-MS and NMR analyses supported guest encapsulation, whereas fluorescence indicated the formation of a 1 : 1 host–guest complex with an association constant of *ca.* 5.4 × 10^4 M^{-1}. Initial experiments to establish efficient hydrogen production indicated that the proton reduction is more efficient at pH of ≈12.6. Then, in a model reaction, H_2S gas was bubbled into a H_2O/EtOH (1 : 5 v/v) solution containing FL (2.0 mM) and NaOH (0.1 mM, to adjust pH to a value of 12.6); this led to a sulfide ion (S^{2-}) concentration of 0.05 M. The mixture was used for hydrogen production under irradiation after addition of the **Ni-TFT** octahedron. The bright yellow-green solution turned turbid with yellow powder and hydrogen gas formed after 24 h of irradiation (Fig. 6b). The yellow powder was filtered off (*ca.* 1 mg) and confirmed to be elemental sulfur by PXRD.

When the fluorescein concentration was held constant (2.0 mM), hydrogen generation increased linearly (from 2.0 μM to 6.0 μM) as a function of **Ni-TFT** concentration (Fig. 6c), indicating that the internal cavity of **Ni-TFT** is required for the decomposition of H_2S at a turnover number of 2600 per mole of MOC catalyst. The preorganization of the dye within **Ni-TFT** results in proximity, allowing for a direct photoinduced electron transfer from the excited state of the FL* dye to the redox catalyst, establishing a Ni(II)/Ni(I) redox center whose reduction potential is well-suited for proton reduction in aqueous media; the latter ultimately reduces the nickel com-

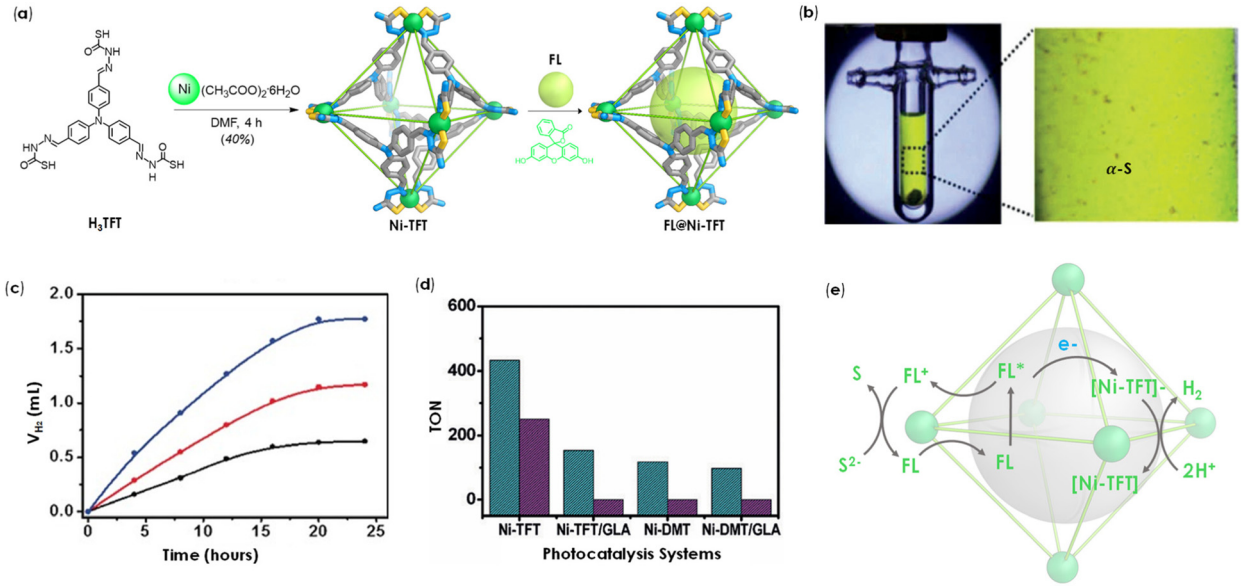

Fig. 6 (a) Self-assembly of **Ni-TFT** and formation of its host–guest complex with Fl. (b) Photographs showing the reaction mixture containing yellowish powder following irradiation. (c) Light-driven hydrogen evolution activity of systems containing FL (2.0 mM), Na_2S (0.05 M) and **Ni-TFT** 2.0 mM (black line), 4.0 mM (red line) and 6.0 mM (blue line). (d) Turnover number of hydrogen (per Ni atoms, green bars) and sulfur (per Ni atoms, purple bar) produced of systems containing FL (2.0 mM)/Na_2S (0.05 M) with **Ni-TFT** (4.0 μM) and **Ni-DMT** (24 μM). (e) Schematic representation for the encapsulation of FL within **Ni-TFT** to produce H_2 and sulfide oxidation from H_2S splitting. Parts (b–e) adapted from ref. 61, https://doi.org/10.1002/anie.201704327. Copyright 2017, Wiley-VCH.

plexes of the cage ([**Ni-TFT**]$^-$), and expels the oxidized FL^+ dye from the molecular cavity. Then, the reduced cage reduces protons to produce molecular hydrogen. With the oxidized dye outside the cage, FL^+ oxidizes sulfide ions in solution to generate the observed yellowish solid sulfur (Fig. 6e). Importantly, the pre-organization of fluorescein within the cavity facilitates a direct photoinduced electron transfer to the redox center, bypassing diffusion limitations and enabling efficient proton reduction. The achieved TON by the design (2600 per mole of catalyst) rivals the reported values for semiconductor photocatalysts under similar conditions. While semiconductor systems such as TiO_2, ZnO, CdS, and ZnS often require noble metal co-catalysts (Pt, Pd, Ir, Ru, Rh, or Au) to trap photogenerated electrons, prolong electron lifetimes, and enhance hydrogen evolution,[62] **Ni-TFT** accomplishes this using an inexpensive, reusable organic dye. This eliminates dependence on costly noble metals, offering a more sustainable approach. Additionally, introducing sulfur atoms into the ligand makes Ni-TFT more stable against sulfide passivation, a common problem in inorganic catalysts. For context, the industrial Claus process for H_2S decomposition requires temperatures above 1000 °C and still achieves low conversion rates, with >50% conversion only at ~1375 °C.[63] In contrast, **Ni-TFT** enables hydrogen evolution from H_2S at room temperature under visible light, highlighting a significant advantage in energy efficiency and operational simplicity. To validate the role of molecular confinement for fluorescein activation and H_2S splitting, a mono-nuclear **Ni-DMT** complex was synthesized by reacting $Ni(CH_3COO)_2{\cdot}4H_2O$ and HDMT. The crystal structure of the complex confirmed that the ligand environment around the nickel(II) atom is similar to that of the metal ions in the **Ni-TFT** cage. Under the same pH, fluorescein and Na_2S concentrations, and using enough molecular **Ni-DMT** to ensure the same nickel atom concentration (24 μM), only 0.32 mL of H_2 gas was generated, and no yellow precipitate was observed. In connection to this, a competitive inhibition experiment was carried out by adding glucosamine (GLA), which competes with FL for the cage interior. The addition of GLA to the original FL (2.0 mM)/**Ni-TFT** (4.0 μM)/Na_2S (0.05 M) reaction system also resulted in only 0.32 mL of H_2 gas and no sulfur formation (Fig. 6d). The confinement effect within the **Ni-TFT** octahedral cage significantly influences the reaction pathway by organizing the dye and catalytic sites within a spatially restricted, electronically modulated environment. The cavity promotes close proximity between the photosensitizer and nickel centers, enabling a direct photoinduced electron transfer through oxidative quenching, which is more efficient than reductive quenching that occurs in bulk solutions. Additionally, the hydrophobic cavity mimics the active sites found in enzymes, selectively favoring proton reduction within the pocket and expelling the oxidized, more polar, and water-soluble dye for sulfide oxidation outside. Together, these results underscore the power of supramolecular confinement in achieving host–guest-mediated photocatalytic redox reactions of gases.

Duan, Jing, and co-workers demonstrated the utility of the host–guest catalyst approach for gas conversion in synthetic chemistry. In this study, the light-driven splitting of H_2S, yielding hydrogen gas, was combined with the subsequent

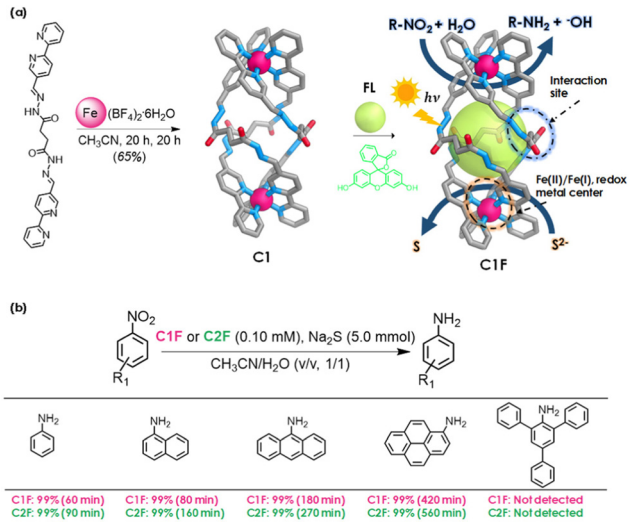

Fig. 7 (a) Schematic representation of self-assembly of **C1** and the photocatalytic system of **C1F** for the combination of H_2S splitting and hydrogenation of nitroaromatics. (b) Photocatalytic reduction of different nitroaromatics into aminoarenes under standard conditions: substrate (0.50 mmol).

reduction of nitroaromatics in a one-pot process (Fig. 7).[64] Two helical $[Fe^{II}_2L_3]^{6+}$ metal–organic capsules, **C1** and **C2**, were synthesized using Fe(II) ions and ligands with or without hydrogen-bonding capabilities. Capsule **C1**, featuring amide groups, was able to encapsulate fluorescein (FL) and form the stable host–guest **C1F** complex through hydrogen bonding (Fig. 7a). Although capsule **C2** lacked such interactions, it also formed the corresponding host–guest **C2F** complex upon encapsulation of fluorescein. Upon photoirradiation, both capsules catalyzed the transformation of H_2S into hydrogen gas and elemental sulfur. The authors hypothesized that incorporating unsaturated substrates within the capsule cavities could enable direct hydrogenation *via* proximity to the generated active hydrogen species. Hence, the produced active hydrogen was utilized for hydrogenation of nitroaromatics, to aniline derivatives (Fig. 7b). Under optimized conditions for hydrogen generation, the reduction of nitrobenzene (0.50 mmol) to aniline was first studied, which directly resulted in the formation of aniline (up to 99% yield) within 60 min. When the concentrations of Na_2S and nitrobenzene were fixed and the **C1F** loading was varied from 0.20 mM to 1.0 mM, the initial reduction rates of nitrobenzene exhibited first-order dependence on the **C1F** concentration. With varying the size of the nitroaromatic from nitrobenzene to 1-nitropyrene, the initial rate decreased from 1.87 mM min^{-1} to 0.28 mM min^{-1}, showing the size-dependent kinetics of the catalytic process, suggesting that the reduction process occurs within the helicate cavity. As evidence of this, when 2,4,6-triphenylnitrobenzene, which has a molecular size larger than the cavity of **C1F**, was used as the substrate, no amine product was observed under the optimized conditions, and only a small amount of hydrogen gas was generated.

Although **C2** showed higher overall photocatalytic efficiency, **C1** exhibited superior performance in the reduction of nitroaromatics, a reaction highly sensitive to substrate size and cavity compatibility. The observed size-dependent kinetics and Michaelis–Menten behavior confirmed that the reactions occurred within the confined space of the capsules, mimicking enzyme-like selectivity. These findings further attest to the potential of molecular confinement in enhancing reactivity and selectivity. The encapsulation of substrates within tailored cavities facilitates pseudo-intramolecular electron transfer, stabilizes reactive intermediates, and enables controlled redox transformations. In particular, the ability of **C1** to selectively bind and transform nitroaromatics highlights how hydrogen bonding and cavity architecture can be leveraged to tune catalytic outcomes. This work exemplifies how supramolecular confinement within MOCs can be harnessed for efficient gas transformation and substrate-specific catalysis, paving the way for coupling cage-based gas conversions to sustainable production of complex and fine chemicals.

Sulfur dioxide (SO_2) is an irritating and highly toxic gas that poses severe health risks to humans, with exposure levels exceeding 100 ppm potentially being fatal. SO_2 is categorized as one of the most hazardous air pollutants,[65] influencing climate change and playing a major role in atmospheric chemistry. Its emissions contribute to the presence of particulate matter ($PM_{2.5}$) and the formation of acid rain, causing damage to crops and forests. Our group has recently noted the essential role of the molecular cavity within **MOC-Pd-NO$_3$** in enhancing the efficiency of the transformation of dry or humid SO_2 gas into sulfate, further emphasizing the importance of cage cavities in optimizing chemical processes.[66] The nanometric **MOC-Pd-NO$_3$** cage results from the self-assembly of the three-fold-symmetric ligand $L(NO_3)_3$ with palladium(II) nitrate in water.[67] SC-XRD analysis revealed a pseudo-cubic $[Pd^{II}_6L_8]^{36+}$ molecular framework, which consists of eight corners defined by an aryl ligand moiety and six faces covered by a Pd^{II} ion coordinated by four pyridyl rings; in this array, the $Pd^{II}\cdots Pd^{II}$ separations range from 1.80 to 2.14 nm. The positive cage charge is balanced by 36 nitrate counterions that reside within the cage interior (Fig. 8a). Activated **MOC-Pd-NO$_3$** can capture up to 6.00 mmol g^{-1} of SO_2 at 298 K and 1.0 bar. Notably, 94% of the captured SO_2 is irreversibly retained (*ca.* 5.70 mmol g^{-1}), as evidenced by the pronounced and broad hysteresis loop observed in the SO_2 isotherms (Fig. 8b). FT-IR, XPS, and NMR analyses confirmed that the retained gas oxidizes to sulfate due to its reaction with cage nitrate ions; all nitrate is consumed. During this process, one cage unit lowers the harmful effects of *ca.* 42 moles of SO_2, in other words, 1.0 gram of cage material can inactivate *ca.* 360 mg of hazardous SO_2 at room temperature. Isostructural MOC-M-NO_3 cages assembled through Co(II), Cu(II), or Zn(II) exhibited SO_2-chemisorption; however, only Pd(II) ions induce quantitative SO_2 conversion. While **MOC-Pd-NO$_3$** oxidizes 94% (*ca.* 5.7 mmol g^{-1}) of its uptake, **MOC-Zn-NO$_3$** decomposes upon exposure to SO_2, and the **MOC-Co-NO$_3$** and **MOC-Cu-NO$_3$** cages achieve partial irreversible adsorption; from what they capture, solely 57% (*ca.*

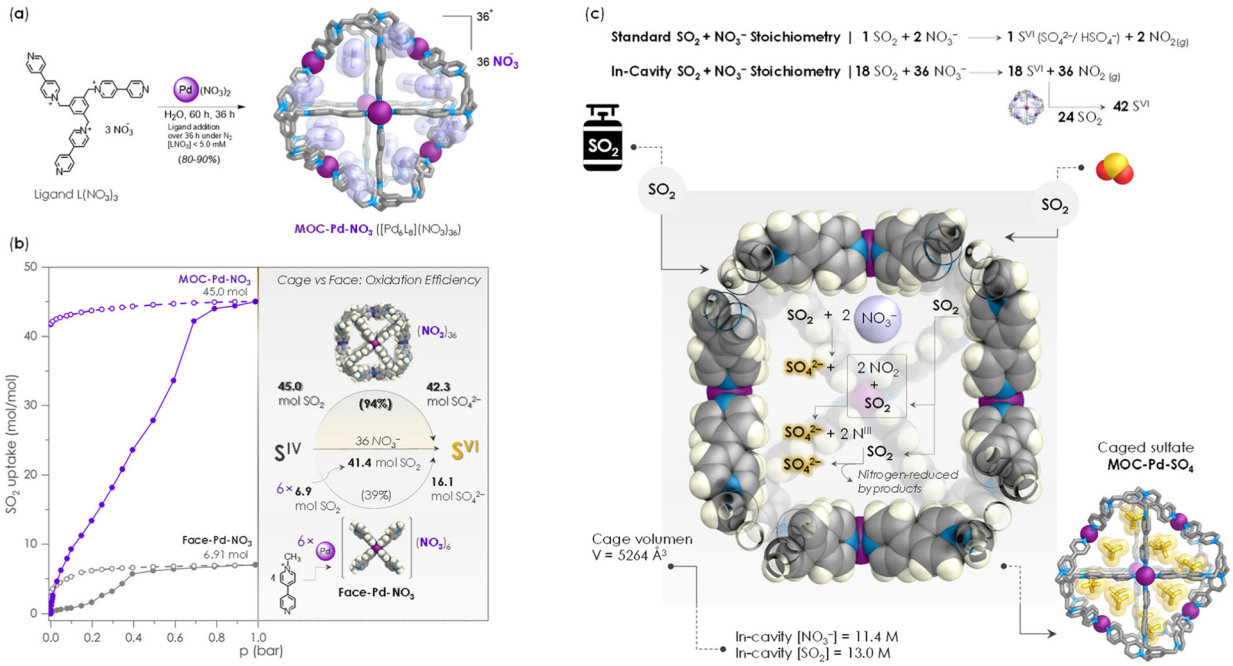

Fig. 8 (a) Aqueous self-assembly of **MOC-Pd-NO$_3$**. The cationic part of the crystal structure of cage is depicted displaying the encapsulated nitrate counterions in space-filling mode. (b) Comparison of the SO_2 uptake of **Face-Pd-NO$_3$** molecular complex against its **MOC-Pd-NO$_3$** cage counterpart; adsorption isotherms at 298 K and up to 1 bar (left). Comparison of the SO_2-oxidation ability of the six-faced **MOC-Pd-NO$_3$** against six disassembled **Face-Pd-NO$_3$** edges (right). (c) Schematic representation of the cavity-mediated mechanism of SO_2 to SO_4^{2-} transformation leading to the formation of **MOC-Pd-SO$_4$** containing trapped sulfate. Part (b) adapted from ref. 66, https://doi.org/10.1002/anie.202421169. Copyright 2025, Wiley-VCH.

1.8 mmol g^{-1}) and 46% (*ca.* 3.0 mmol g^{-1}) are chemisorbed, respectively.

The cage cavity was identified as the most significant factor in efficient sulfate formation. A molecular **Face-Pd-NO$_3$** complex, representing one edge of the cage, was prepared and exposed to SO_2, resulting in an adsorption of 6.91 mol of SO_2 per mol of complex. As expected, this amount is one-sixth of the uptake observed with **MOC-Pd-NO$_3$** (45.0 mol mol^{-1}). In this context, six moles of **Face-Pd-NO$_3$** complex, which are equivalent to one mol of the **MOC-Pd-NO$_3$** cage and provide a total of 36 nitrates, collectively achieve an uptake of 41.4 moles of SO_2. However, only about 39% of the SO_2 adsorbed by **Face-Pd-NO$_3$** was chemisorbed, and a significant amount of unreacted NO_3^- was detected. Although six molecular edges adsorb virtually the same amount of gas as the six faces forming the cage (41.4 compared to 45 moles), only 16.1 moles of SO_2 would be oxidized by six separated edges. This yield is quite poor when compared to the 42.3 moles of gas converted by the pseudo-cube (94% yield of S(IV) to S(VI) oxidation, Fig. 8b).

Based on the results and the established chemistry surrounding the reaction of SO_2 by nitrate,[68] a cavity-mediated mechanism for in-cage sulfate production was proposed (Fig. 8c). Initially, SO_2 diffuses into the cage, where it may react with the confined nitrates according to the standard 1 SO_2 : 2 NO_3^- stoichiometry, yielding one equivalent of sulfate and two of NO_2. The NO_2 gaseous product is a strong SO_2 oxidant and can react with additional gas, producing more sulfate and N^{III}-reduced species, which may continue to oxidize SO_2 until cage saturation. The nanoconfined environment of the cage enforces highly effective concentrations of reactants. It is estimated that the effective concentrations of nitrate and SO_2 could reach up to 11.4 and 13.3 M per cage, respectively, based on a molecular volume of 5264 $Å^3$. Likewise, the inner cage space may act as a reservoir for the gaseous byproduct NO_2 and stabilize reactive intermediates, many of which are likely to be radicals. The synergistic operation of these effects resulted in the observation of an unprecedented *ca.* 2.3 SO_2 : 2 NO_3^- stoichiometry (42 SO_2 : 36 NO_3^-), significantly exceeding the established 1 SO_2 : 2 NO_3^- standard ratio. Finally, immersing the solid product **MOC-Pd-SO$_4$** in water, followed by the addition of $Ba(NO_3)_2$, brought about the regeneration and release of caged sulfate into solution, its precipitation as $BaSO_4$, and the recycling of former nitrate cage, **MOC-Pd-NO$_3$**.

From the discussed examples, it is evident that metal–organic cages can be regarded as emerging catalytic platforms for gas conversion reactions, leveraging their confined cavities to influence reactivity and selectivity. The spatial confinement within these discrete constructs enables unique mechanistic pathways, stabilizes reactive intermediates, and enhances local concentrations of substrates. Table 1 summarizes the features of the examples discussed, highlighting their catalytic roles, operating conditions, and key mechanistic insights that underpin their performance in gas transformations.

Table 1 Key aspects and mechanistic insights of gas conversion reactions within MOCs

MOC catalyst	Gas transformation	General conditions	Yields/selectivity	Key mechanistic insights	Ref.
Co_{14}(L-CH_3)$_{24}$ (a $[Co^{II}_{14}L_{24}]^{4+}$ MOC)	Photocatalytic $O_2 + H_2O \rightarrow H_2O_2$	UV/Vis–NIR (λ = 300–1100 nm), O_2-saturated water, no sacrificial agent	H_2O_2 (production rate = 146.6 mol g^{-1} h^{-1})	Photogenerated e^- reduce O_2 (ORR); h^+ oxidize H_2O (WOR); both *via* 2e^- processes	53
BIC-145 (a $[Cu^{I}_{6}L_4]^{2+}$ MOC)	Electrochemical reduction $CO_2 \rightarrow C_2H_4$ (main)	Electrocatalysis in KCl : CS_2CO_3, CO_2 flow, −1.2 V	FE: 28% for C_2H_4 and current density of −3.54 mA cm^{-2} Minor products: CO, CH_4, HCOOH	Cu(I) sites enable *CO/*CHO coupling; cage stabilizes intermediates	54
Im-PL-Cage (Zn-calixarene/imidazolium MOC as a porous liquid)	*N*-formylation CO_2 + morpholine → *N*-formylmorpholine	1.0 bar CO_2, phenylsilane, DMF, 60 °C, 10 h	7.74 mmol of CO_2 to formylation product (96.7% yield)	PEG chains enhance CO_2 transport and storage; imidazole sites activate CO_2	55
Cu_4I_4@Cu_3VMOP (host–guest catalyst [Cu_3VMOP (Cu_4I_4)]$^{4-}$)	Photoreduction $CO_2 \rightarrow$ HCOOH	CH_3CN, $Ru(bpy)_3Cl_2$, triethanolamine, light	10.5 mmol g^{-1} of HCOOH product; 100% selectivity	Cu_4I_4 cluster improves charge separation; lowers energy barrier for HCOOH formation over CH_3COOH	56
H1 (host–guest catalyst, $[Fe^{II}_4L_4(MEACO)_2]^{8+}$)	Electrochemical reduction $CO_2 \rightarrow CH_4$	H-type cell, RT, ethanolamine, LiCl, DMSO/H_2O (2 : 1), CO_2 (saturation)	CH_4 selectivity ≈100%; FE = 69.8%; TON > 220; TOF ≈ 35 h^{-1}	H1 encapsulates ethanolamine, yielding H1-$MEACO_2$ guest adduct and lowering the reduction potential of CO_2. Guest hydrogenation forms $MEACH_3$*. The C–N bond is broken releasing CH_4.	60
Ni-TFT ([$Ni^{II}_6L_4$(fluorescein)] host–guest catalyst)	Photocatalytic splitting and H_2 generation $H_2S \rightarrow H_2 + S$	pH ≈ 12.6, Ni-TFT (4 μM), fluorescein, Et_3N, H_2O/EtOH, Na_2S (0.05 M)	H_2 and elemental sulfur obtained (1 mg). TON: 1600 for H_2	Light-activated fluorescein is expelled from the cavity and oxidizes S^{2-}; Ni center reduces protons to H_2	61
C1F (a triple helical $[Fe^{II}_2L_2$(fluorescein)]$^{4+}$ host–guest catalyst)	Photocatalytic H_2 generation $H_2S \rightarrow H_2 + S$; then, nitroaromatic reduction	CH_3CN/H_2O, Na_2S, Xe lamp	H_2 (TON: 276.7; TOF: 19.7 h^-); 0.05 mmol aniline products	Fluorescein activation; H_2 reduces nitroaromatics; ouside of the cavity, the oxidized fluorescein oxidizes S^{2-}	64
MOC-Pd-NO_3 (a pseudocubic $[Pd^{II}_6L_8]^{36+}$ catalyst)	Redox gas reaction $SO_2 + NO_3^- \rightarrow SO_4^{2-}$	Solid-state, 1.0 bar SO_2, 298 K	5.7 mmol of SO_4^{2-} produced per gram of MOC (94% conversion efficiency)	NO_3^- ions oxidize SO_2, yielding SO_4^{2-} and reduced nitrogenate species. Efficiency given by both Pd and MOC cavity (increases reactant concentrations)	66

FE: faradaic efficiency

Considering the discussion presented, it is important to note that reticular MOFs and COFs have been studied more extensively than discrete MOCs concerning gas capture and their chemical transformation, and each of these systems brings distinctive strengths and faces specific limitations in gas transformation. Undoubtedly, MOFs have been protagonist materials in this century, they are known for their ultrahigh surface areas, crystalline long-range order, and versatile metal chemistry that facilitates adsorption and heterogeneous catalysis, though their performance can be constrained by moisture/chemical stability, activation requirements, as well as gas diffusion and mass transport into the deepest pores. COFs exhibit covalent backbone robustness, thermal stability, and organic pore environments that can be tailored for selective adsorption and photocatalysis; yet, challenges remain in achieving the required high crystallinity, controlling interlayer stacking, and enhancing the catalytic conversion of gases, as they lack metal sites.

Meanwhile, MOCs can be solubilized in organic solvent or water, ideal for homogeneous catalysis and monitoring of host–guest interactions. As porosity is intrinsic to the molecule, crystalline material is not mandatory for gas capture and conversion; activity is seen for MOCs as dissolved molecules, crystalline-ordered, or amorphous solids. However, concerns regarding scalability and long-term cage integrity persist today. MOCs usually display lower thermal, hydrolytic, and chemical stability than MOFs and COFs; current and continuous efforts are helping mitigate these limitations. Rather than positioning MOCs as "better" materials, this contribution also intended to point out that MOCs complement current reticular materials and broaden the toolbox for gas conversion using porous systems.

Research on gas conversion using MOCs remains scarce compared to MOFs or COFs; however, MOCs have demonstrated strong potential as catalytic platforms, not only complementing but often matching or even surpassing the activity of reticular materials. Their unique molecular nature and solubility introduce additional effects not observed in solid frameworks. In particular, the solubility of many MOCs enhances host–guest interactions with gases and other substrates, as exemplified by systems involving fluorescein and nitroaromatics. Furthermore, cage solubility facilitates guest diffusion

and retention within the cavity, enabling in-cage formation of cocatalysts, such as the Cu_4I_4 cluster or the ethanolamine–CO_2 adduct, whose confinement within the cage significantly improves gas conversion efficiency.

Such possibilities have been illustrated in this contribution. For example, CO_2 reduction using **Cu_4I_4@Cu_3VMOP** (containing the endogenous Cu_4I_4 cluster) achieved 100% selectivity toward HCOOH. This performance surpasses that of other MOFs, such as the Sn(II)-doped ZIF-8 reported by Geng *et al.*,[69] which reached 74% selectivity for HCOOH formation, and the dual-MOF copper-based catalytic electrode developed by Liu *et al.*,[70] which exhibited 90% efficiency for selective HCOOH production.

Only a few MOFs have been reported to adsorb H_2S and convert it into sulfides–typically as an unintended consequence. Most MOFs capable of adsorbing this polar, acidic gas suffer from poor chemical stability, often forming irreversible metal–sulfur bonds and metal sulfides (evidenced by black solids such as ZnS, CuS, or FeS), leading to cluster disintegration or partial structural collapse. These degradations are generally accelerated by the presence of water.[71,72] Distinct from this behavior, the molecular cage **Ni-TFT** photocatalytically decomposes H_2S in aqueous solution into hydrogen and elemental sulfur without cage decomposition or NiS formation. Another example of how MOCs can exhibit unique reactivity compared to MOFs or COFs is **MOC-Pd-NO_3**, where nitrate counterions and confined molecular space promote SO_2 oxidation to sulfate. Cage integrity is maintained thanks to its solubility and anion-exchange capability. Currently, the efficient, quantitative, and clean conversion of SO_2 into more benign and useful byproducts, while allowing for adsorbent recovery, is unparalleled in the state-of-the-art of reticular or molecular gas adsorbents such as MOFs, COFs, HBFs, or POCs.

3. Conclusions

The examples discussed in this contribution underscore the remarkable potential of MOCs as platforms for the capture and chemical transformation of gases into value-added products. By mimicking the selective and efficient microenvironments of enzymes, MOCs offer a unique opportunity to extend host–guest chemistry to gaseous substrates, permitting transformations that are both catalytically improved and spatially controlled, and may take place in gas–liquid–solid phase. Across the systems examined, it is evident that molecular confinement and the ability of cage cavities to encapsulate gases, catalysts, and co-substrates are central to increasing reactivity and selectivity. These confined environments stabilize reactive intermediates, preorganize molecular components, and enforce intramolecular electron transfer, all of which contribute to improved catalytic performance. The size, shape, and functionalization of the cavity directly influence substrate accessibility, intermediate stabilization, and reaction pathways, making confinement a key design principle for gas-phase catalysis.

The examples discussed herein highlight key structural features that render MOCs suitable for gas conversions. These features can be regarded as design principles for developing novel gas transformations within the molecular interiors of MOCs: (1) cavity: accessible internal cavities of appropriate dimensions enable gas diffusion, substrate accommodation, and size selectivity. Larger ligands can increase pore volume, improving catalytic performance for bulkier substrates and allowing co-catalyst encapsulation. A balance between size and polarity is crucial: enclosed polar environments within cages promote CO_2 capture, enhance affinity for polar gases (*e.g.*, H_2S, SO_2), and influence selectivity for polar intermediates and products.

(2) Stability: robust frameworks that maintain integrity under harsh catalytic conditions-including aqueous environments, wide pH ranges, high temperature, or corrosive species-are essential. Metal nodes dictate coordination geometry and stability; thus, kinetically inert metals should be considered to ensure resistance under acidic, basic, or high-temperature conditions. Rigid, bulky metal nodes further prevent degradation in the working medium.[73]

(3) Metal centers: in some cases, metal sites of the cage framework have been observed to play a pivotal role in gas conversion by activating substrates, stabilizing intermediates, and enabling redox processes. Open-metal sites that coordinate and immobilize gaseous guests within the cage should allow labile metal–ligand bonds and ligand exchange without compromising structural integrity. This can be achieved using metals with flexible coordination geometries (*e.g.*, Zn(II), Co(II), Cu(II)). Metals that exhibit multiple oxidation states (such as Fe(III)/Fe(II), Ni(II)/Ni(I), or Cu(II)/Cu(I)) and have labile coordination sites may facilitate electron transfer and substrate exchange.

(4) Functionalized ligands: organic ligands define the shape and polarity, and influence the stability of MOCs through the number of their coordination sites (*e.g.*, ditopic, tritopic, tetratopic). Functionalization is thus essential for host–guest recognition and molecular preorganization. Introducing hydrogen-bond donors/acceptors, aromatic centers, or charged groups enhances substrate binding *via* hydrogen bonding or π-stacking interactions. Additionally, ligands should possess a degree of flexibility to allow for dynamic complex formation; incorporating methylene groups or weakly coordinating amines can provide this necessary adaptability. In summary, rational MOC design requires balancing structural stability with dynamic adaptability, optimizing metal–ligand interactions, and tailoring cavity size and polarity to achieve high catalytic efficiency and selectivity.

While the use of MOCs for gas conversion is still in its early stages, the results presented here highlight their promise and versatility. We anticipate that future advances will focus on stimuli-responsive or adaptive cages, capable of dynamically adjusting cavity size, polarity, or functionality to accommodate diverse gases and intermediates. Moreover, the development of multifunctional cages that co-encapsulate catalysts, photosensitizers, and substrates could allow tandem or cascade reac-

tions, further expanding the scope of MOC-based catalysis. In this sense, the integration of computational tools for guided design will be helpful to predict host–guest interactions and optimize cavity environments for specific gas reactions. Additionally, finding methods for embedding MOCs into hybrid catalytic materials—such as porous liquids, catalytic membranes, flow reactors or electrodes[74,75]—will enhance scalability, recyclability, and process integration,[76] moving beyond gas capture toward gas conversions.

Ultimately, the field of gas transformations using porous materials and molecular cages holds immense potential for environmental remediation, energy storage, and sustainable chemical synthesis. By enabling the selective conversion of reactive, harmful, pollutant gases into useful products such as fuels, fine chemicals, or fertilizers, MOCs offer a promising route toward green and circular chemical processes, positioning them as versatile platforms for addressing some of the global challenges in pollution control and renewable energy.

Conflicts of interest

There are no conflicts to declare.

Data availability

No primary research results, software or code have been included and no new data were generated or analyzed as part of this review.

Acknowledgements

This work was supported by the Dirección General de Asuntos del Personal Académico from the DGAPA UNAM-PAPIIT program, Mexico (grant IN212223). F. T. T. is grateful to SECIHTI Mexico for a graduate scholarship (CVU 2038873, grant number 4047239).

References

1 Y.-L. Zhao, X. Zhang, M.-Z. Li and J.-R. Li, *Chem. Soc. Rev.*, 2024, **53**, 2056.
2 L. F. Vega, D. Bahamon and I. I. I. Alkhatib, *ACS Sustainable Chem. Eng.*, 2024, **12**, 5357.
3 M. Yousaf, M. Zaman, A. Mahmood, M. Imran, A. Elkamel, M. Rizwan, T. Wilberforce and F. Riaz, *Energy Sci. Eng.*, 2022, **10**, 4890.
4 B. Yao, T. Xiao, O. A. Makgae, X. Jie, S. Gonzalez-Cortes, S. Guan, A. I. Kirkland, J. R. Dilworth, H. A. Al-Megren, S. M. Alshihri, P. J. Dobson, G. P. Owen, J. M. Thomas and P. P. Edwards, *Nat. Commun.*, 2020, **11**, 6395.
5 L. Zhang, C. Wang and C. Zhan, *Mater. Chem. Front.*, 2025, **9**, 1650.
6 A. Jana, A. Maity, A. Adalder, S. Saha and A. Bhunia, *Nanoscale*, 2025, **17**, 12235.
7 W. Shan, Z. Wang, C. Gao, X. Li, W. Zhuang, R. Liu, C. Shi, H. Qin, X. Li and D. Shi, *Green Chem.*, 2024, **26**, 5744.
8 J. Gandara-Loe, L. Pastor-Perez, L. F. Bobadilla, J. A. Odriozola and T. R. Reina, *React. Chem. Eng.*, 2021, **6**, 787.
9 J. G. Doremus, B. Lotsi, A. Sharma and P. L. McGrier, *Nanoscale*, 2024, **16**, 21619.
10 Q. Song, Z. Li, Q. Peng, X. Ou, K. Zhao, Z. Dong, L. Ye, C. Liu, Y. Liu, J. He, L.-H. Chung and B. Han, *Appl. Catal., B*, 2025, **378**, 125619.
11 Y. Li, J. Zhang, K. Zuo, Z. Li, Y. Wang, H. Hu, C. Zeng, H. Xu, B. Wang and Y. Gao, *Angew. Chem., Int. Ed.*, 2024, **63**, e202405476.
12 S. Zhang, Y. Zhuo, C. I. Ezugwu, C.-C. Wang, C. Li and S. Liu, *Environ. Sci. Technol.*, 2021, **55**, 8341.
13 Z. Alsudairy, N. Brown, A. Campbell, A. Ambus, B. Brown, K. Smith-Petty and X. Li, *Mater. Chem. Front.*, 2023, **7**, 3298.
14 J. Song, Z. Zhang, S. Hu, T. Wu, T. Jiang and B. Han, *Green Chem.*, 2009, **11**, 1031.
15 H. Xu, X.-F. Liu, C.-S. Cao, B. Zhao, P. Cheng and L.-N. He, *Adv. Sci.*, 2016, **3**, 1600048.
16 D. Zhao, X.-H. Liu, C. Zhu, Y.-S. Kang, P. Wang, Z. Shi, Y. Lu and W.-Y. Sun, *ChemCatChem*, 2017, **9**, 4598.
17 W.-Y. Gao, H. Wu, K. Leng, Y. Sun and S. Ma, *Angew. Chem., Int. Ed.*, 2016, **55**, 5472.
18 R. Chakrabarty, P. S. Mukherjee and P. J. Stang, *Chem. Rev.*, 2011, **111**, 6810.
19 T. R. Cook and P. J. Stang, *Chem. Rev.*, 2015, **115**, 7001.
20 A. J. McConnell, *Chem. Soc. Rev.*, 2022, **51**, 2957.
21 E. G. Percástegui, T. K. Ronson and J. R. Nitschke, *Chem. Rev.*, 2020, **120**, 13480.
22 F. J. Rizzuto, L. K. S. von Krbek and J. R. Nitschke, *Nat. Rev. Chem.*, 2019, **3**, 204.
23 E. G. Percástegui, *Eur. J. Inorg. Chem.*, 2021, **2021**, 4425.
24 M. D. Ward, C. A. Hunter and N. H. Williams, *Acc. Chem. Res.*, 2018, **51**, 2073.
25 T. Y. Kim, R. A. S. Vasdev, D. Preston and J. D. Crowley, *Chem. – Eur. J.*, 2018, **24**, 14878.
26 S. Cruz-Nava, S. de J. Valencia-Loza and E. G. Percástegui, *Eur. J. Org. Chem.*, 2022, e202200844.
27 M. Yoshizawa and L. Catti, *Acc. Chem. Res.*, 2019, **52**, 2392.
28 A. Brzechwa-Chodzyńska, W. Drożdż, J. Harrowfield and A. R. Stefankiewicz, *Coord. Chem. Rev.*, 2021, **434**, 213820.
29 A. J. Plajer, E. G. Percástegui, M. Santella, F. J. Rizzuto, Q. Gan, B. W. Laursen and J. R. Nitschke, *Angew. Chem., Int. Ed.*, 2019, **58**, 4200.
30 N. Dey and C. J. E. Haynes, *ChemPlusChem*, 2021, **86**, 418.
31 C. García-Simón, M. Garcia-Borràs, L. Gómez, T. Parella, S. Osuna, J. Juanhuix, I. Imaz, D. Maspoch, M. Costas and X. Ribas, *Nat. Commun.*, 2014, **5**, 5557.
32 K. Wu, K. Li, Y.-J. Hou, M. Pan, L.-Y. Zhang, L. Chen and C.-Y. Su, *Nat. Commun.*, 2016, **7**, 10487.

33 T. Grancha, A. Carné-Sánchez, L. Hernández-López, J. Albalad, I. Imaz, J. Juanhuix and D. Maspoch, *J. Am. Chem. Soc.*, 2019, **141**, 18349.
34 S. K. Samanta, D. Moncelet, V. Briken and L. Isaacs, *J. Am. Chem. Soc.*, 2016, **138**, 14488.
35 Y.-R. Zheng, K. Suntharalingam, T. C. Johnstone and S. J. Lippard, *Chem. Sci.*, 2015, **6**, 1189.
36 G. Montà-Gongález, D. Bastante-Rodríguez, A. García-Fernández, P. J. Lusby, R. Martínez-Máñez and V. Martí-Centelles, *Chem. Sci.*, 2024, **15**, 10010.
37 G. Montà-González, R. Martínez-Máñez and V. Martí-Centelles, *Targets*, 2024, **2**, 372.
38 E. G. Percástegui, *Chem. Commun.*, 2022, **58**, 5055.
39 Y. Gao, S.-Q. Deng, X. Jin, S.-L. Cai, S.-R. Zheng and W.-G. Zhang, *Chem. Eng. J.*, 2019, **357**, 129.
40 D. Camdzic, H. K. Welgama, M. R. Crawley, A. Avasthi, T. R. Cook and D. S. Aga, *ACS Appl. Eng. Mater.*, 2024, **2**, 87.
41 Q.-W. Zeng, L. Hu, Y. Niu, D. Wang, Y. Kang, H. Jia, W.-T. Dou and L. Xu, *Chem. Commun.*, 2024, **60**, 3469.
42 W. Li, L. Wang, B. E. Keshta, Y. Bi, Y. Zhang and B. Chen, *Coord. Chem. Rev.*, 2025, **545**, 217032.
43 J.-L. Zhu, D. Zhang, T. K. Ronson, W. Wang, L. Xu, H.-B. Yang and J. R. Nitschke, *Angew. Chem., Int. Ed.*, 2021, **60**, 11789.
44 C. A. Rowland, G. R. Lorzing, A. J. Gosselin, B. A. Trump, G. P. A. Yap, C. M. Brown and E. D. Bloch, *J. Am. Chem. Soc.*, 2018, **140**, 11153.
45 A. Carné-Sánchez, J. Martínez-Esaín, T. Rookard, C. J. Flood, J. Faraudo, K. C. Stylianou and D. Maspoch, *ACS Appl. Mater. Interfaces*, 2023, **15**, 6747.
46 G. R. Lorzing, A. J. Gosselin, B. A. Trump, A. H. P. York, A. Sturluson, C. A. Rowland, G. P. A. Yap, C. M. Brown, C. M. Simon and E. D. Bloch, *J. Am. Chem. Soc.*, 2019, **141**, 12128.
47 X. Feng, X. Wang, H. Yan, H. Liu, X. Liu, J. Guan, Y. Lu, W. Fan, Q. Yue and D. Sun, *Angew. Chem., Int. Ed.*, 2024, **63**, e202407240.
48 W. Liu and J. F. Stoddart, *Chem*, 2021, **7**, 919.
49 H. Takezawa, K. Shitozawa and M. Fujita, *Nat. Chem.*, 2020, **12**, 574.
50 M. Morimoto, S. M. Bierschenk, K. T. Xia, R. G. Bergman, K. N. Raymond and F. D. Toste, *Nat. Catal.*, 2020, **3**, 969.
51 L.-D. Syntrivanis and K. Tiefenbacher, *Angew. Chem., Int. Ed.*, 2024, **63**, e202412622.
52 S. Bhattacharyya, M. R. Black and D. S. Pilgrim, *Chem. Sci.*, 2025, **16**, 21238.
53 J.-N. Lu, J.-J. Liu, L.-Z. Dong, J.-M. Lin, F. Yu, J. Liu and Y.-Q. Lan, *Angew. Chem., Int. Ed.*, 2023, **62**, e202308505.
54 J.-Q. Chen, Q.-H. Li, Q.-L. Hong, P. Shao, H.-X. Zhang and J. Zhang, *Sci. China: Chem.*, 2025, **68**, 943.
55 C. He, Y.-H. Zou, D.-H. Si, Z.-A. Chen, T.-F. Liu, R. Cao and Y.-B. Huang, *Nat. Commun.*, 2023, **14**, 3317.
56 Y. Yang, M. Dong, Q. Wu, C. Qin, W. Chen, Y. Geng, S. Wu, C. Sun, K. Shao, Z. Su and X. Wang, *Angew. Chem., Int. Ed.*, 2025, **64**, e202423018.
57 Y. Wang, E. Chen and J. Tang, *ACS Catal.*, 2022, **12**, 7300.
58 Y.-L. Lu, Y.-P. Wang, K. Wu, M. Pan and C.-Y. Su, *Acc. Chem. Res.*, 2024, **57**, 3277.
59 S. Ganta, J.-H. Borter, C. Drechsler, J. J. Holstein, D. Schwarzer and G. H. Clever, *Org. Chem. Front.*, 2022, **9**, 5485.
60 Z. Zhang, Y. Yang, J. Wang, X. Jing and C. Duan, *Inorg. Chem. Front.*, 2025, **12**, 5389.
61 X. Jing, Y. Yang, C. He, Z. Chang, J. N. H. Reek and C. Duan, *Angew. Chem., Int. Ed.*, 2017, **56**, 11759.
62 G. Ma, H. Yan, X. Zong, B. Ma, H. Jiang, F. Wen and C. Li, *Chin. J. Catal.*, 2008, **29**, 313.
63 W. Mulewa and M. Tahir, *Energy Fuels*, 2024, **38**, 15972.
64 Y. Yang, H. Li, X. Jing, Y. Wu, Y. Shi and C. Duan, *Chem. Commun.*, 2022, **58**, 807.
65 S. J. Smith, J. van Aardenne, Z. Klimont, R. J. Andres, A. Volke and S. Delgado Arias, *Atmos. Chem. Phys.*, 2011, **11**, 1101.
66 E. G. Percástegui, E. Sánchez-González, S. de J. Valencia-Loza, S. Cruz-Nava, V. Jancik and D. Martínez-Otero, *Angew. Chem., Int. Ed.*, 2025, **64**, e202421169.
67 S. de J. Valencia-Loza, A. López-Olvera, E. Martínez-Ahumada, D. Martínez-Otero, I. A. Ibarra, V. Jancik and E. G. Percástegui, *ACS Appl. Mater. Interfaces*, 2021, **13**, 18658.
68 T. Liu, A. W. H. Chan and J. P. D. Abbatt, *Environ. Sci. Technol.*, 2021, **55**, 4227.
69 W. Geng, W. Chen, G. Li, X. Dong, Y. Song, W. Wei and Y. Sun, *ChemSusChem*, 2020, **13**, 4035.
70 S. Liu, L. Song, R. Liu, L. Li, D. Yang, S. Yuan and X. Dai, *Small*, 2023, **19**, 2304808.
71 E. Martínez-Ahumada, A. López-Olvera, V. Jancik, J. E. Sánchez-Bautista, E. González-Zamora, V. Martis, D. R. Williams and I. A. Ibarra, *Organometallics*, 2020, **39**, 883.
72 A. López-Olvera, J. G. Flores, J. Aguilar-Pliego, C. K. Brozek, A. Gutiérrez-Alejandre and I. A. Ibarra, *Chem. Mater.*, 2021, **33**, 6269.
73 M.-T. Lv, M.-D. Cui, K.-P. Bai, Y. Jiang, W.-P. Chen, N.-N. Sun, X.-Q. Hu, C. Huang, Q.-Y. Yang and Y.-Z. Zheng, *Angew. Chem., Int. Ed.*, 2025, **64**, e202506838.
74 L. Rao, X. Zhang, P. Liu, W.-T. Dou, H.-Y. Lin, F. Zhao, W. Zhu, X. Qian, H.-B. Yang and L. Xu, *J. Am. Chem. Soc.*, 2025, **147**, 31618.
75 H.-Y. Lin, L.-Y. Zhou, F. Mei, W.-T. Dou, L. Hu, H.-B. Yang and L. Xu, *Angew. Chem., Int. Ed.*, 2023, **62**, e202301900.
76 T. Jin, K. Zeng, X. Zhang, W.-T. Dou, L. Hu, D. Zhang, W. Zhu, X. Qian, H.-B. Yang and L. Xu, *Angew. Chem., Int. Ed.*, 2024, **63**, e202409878.

